Pore-scale dissolution of $CO_2 + SO_2$ in deep saline aquifers

Saeed Ovaysi*, Mohammad Piri

Department of Chemical and Petroleum Engineering, University of Wyoming, Laramie, WY 82071-2000, USA

ARTICLE INFO

ABSTRACT

We employ Modified Moving Particle Semi-implicit (MMPS) method to study the multi-ion transport of CO_2 and SO_2 in natural porous media at the pore level. A new approach has been developed to account for the electrostatic forces. Compared to solving the Poisson–Nernst–Planck equations, this new approach eliminates the restrictions on the size of time step and hence allows for faster simulations. We carry out a series of simulations to study the dissolution of different charged and neutral species resulting from the injection of pure CO_2 and $CO_2 + SO_2$ in two sandstones, namely Berea and Bentheimer. The pressure, temperature and salinity conditions resemble those encountered in deep saline aquifers and non-ideality of the solution is taken into account by using the Davies activity model. We investigate the impact of pore-space topology on the dispersion of different ions in both cases of pure CO_2 injection and $CO_2 + SO_2$ co-injection. Impact of the electrostatic forces on distribution of different ions in the samples is thoroughly studied.

1. Introduction

Reducing the rate of anthropogenic CO_2 release to the atmosphere is considered an important step toward mitigating global warming and its unwanted consequences. Given the intense reliance of industrial development on fossil fuels, the most viable strategy in this regard seems to be CO_2 capture and storage technology. Among the possible storage scenarios, CO_2 injection into saline aquifers is the most promising. The injected CO_2 to deep saline aquifers can (1) flow updip and accumulate beneath the caprock (structural trapping), (2) migrate into the brine phase and become trapped in the form of isolated clusters (hydrodynamic trapping), (3) dissolve in the brine phase (solubility trapping), and (4) react with the formation minerals to precipitate secondary minerals (mineral trapping). Pore-scale complexities of the formation are among the key players determining the contribution of each of the aforementioned trapping processes on the final fate of the injected CO_2. Therefore, thorough understanding of the pore-scale phenomena pertinent to CO_2 injection in deep saline aquifers is a prerequisite to secure CO_2 sequestration.

Despite the abundance of continuum scale modeling studies of different CO_2 trapping processes, pore-scale studies are few. Moreover, the properties provided by pore-scale models are critical for the continuum scale models. Among the few pore-scale modeling studies on the solubility trapping mechanism in CO_2 sequestration one can point to the studies by Kang et al. (2005), Flukiger and

Bernard (2009), and Li et al. (2008) where lattice-Boltzmann and finite volume techniques are used. Additionally, Lopez et al. (2011) used pore-network modeling to study hydrodynamic trapping of CO_2 in reconstructed sandstones.

The aim of this paper is to shed light on the pore-scale complexities of the solubility trapping process which is a precursor to the more long-term mineral trapping process. To do that we use Modified Moving Particle Semi-implicit (MMPS) technique which we have developed earlier (Ovaysi and Piri, 2010). MMPS is a Lagrangian particle-based method used to model pore-scale fluid flow directly in high-resolution images of naturally occurring porous media. In the present work, we add reaction and ion-transport layers on top of the already existing convection–diffusion model (Ovaysi and Piri, 2011). The model is then used to simulate pore-scale CO_2 and SO_2 solubility trapping in saline aquifers. We start by introducing the porous media used in this work. Then we discuss our ion-transport model along with a brief introduction to MMPS. The presentation will then be followed by the results section where we apply the model on the pore-scale images acquired through microtomography imaging.

2. Pore space representation

We use high-resolution images of two naturally occurring sandstones, Berea and Bentheimer, acquired using computed microtomography. The Berea image (Dong, 2007) has 5.345 μm resolution and, with 400 × 400 × 400 voxels dimension, amounts to (2.138 mm³). The Bentheimer image consists of 670 × 670 × 1500 voxels with 6.007 μm resolution which measures 4.025 mm × 4.025 mm × 9.011 mm in x, y, and z directions,

* Corresponding author. Tel.: +1 307 766 4923; fax: +1 307 766 6777.
  E-mail addresses: sovaysi@uwyo.edu (S. Ovaysi), mpiri@uwyo.edu (M. Piri).

respectively. The Berea sandstone has a 19.6% porosity and 1.2 D permeability whereas our core-scale measurements on the Bentheimer sandstone revealed a 22.2% porosity and 2.7 D permeability.

To make the simulations computationally less expensive, we work with two 0.51 mm × 0.51 mm × 1.09 mm samples (one from each sandstone). Since MMPS is a particle-based method, we assign a particle to each voxel. The microtomography image is then used as a template to mark the solid and void particles. Fig. 1 illustrates the particle representation of the void space for samples A and B from the Berea and Bentheimer sandstones, respectively. Both the solid and void particles take part in MMPS calculations. However, to emphasize on the pore-scale features, we only visualize the void (fluid) particles. Further details of these samples are listed in Table 1.

3. Model description

The first step to modeling the reactive transport of CO_2 in saline aquifers at the pore scale is the solution of the incompressible Navier–Stokes equations, i.e.,

$$\frac{D\mathbf{v}}{Dt} = -\frac{1}{\rho}\nabla P + \frac{\mu}{\rho}\nabla^2\mathbf{v} + \mathbf{g} \tag{1}$$

Table 1
Main features of the two samples taken from the Berea and Bentheimer sandstones studied in this work.

Sample	A	B
Sandstone	Berea	Bentheimer
Number of voxels in X direction	96	85
Number of voxels in Y direction	96	85
Number of voxels in Z direction	204	181
Resolution (μm)	5.345	6.007
Sample size in X direction (mm)	0.51312	0.510595
Sample size in Y direction (mm)	0.51312	0.510595
Sample size in Z direction (mm)	1.09038	1.087267
Sample volume (mm³)	0.28709	0.28346
Total number of main domain particles (solid and fluid)	1,880,064	1,307,725
Total number of particles (solid and fluid) including shell, stabilizer and upstream and downstream	2,519,424	1,880,064
Kernel size (μm)	16.035	18.021

$$\nabla \cdot \mathbf{v} = 0 \tag{2}$$

where $\mathbf{v}$ is the velocity vector, ρ is density, μ is viscosity, $\mathbf{g}$ is the gravity vector, and P is pressure.

We use MMPS to solve Eqs. (1) and (2) for the porous media presented in Section 2. The advantages of using a Lagrangian
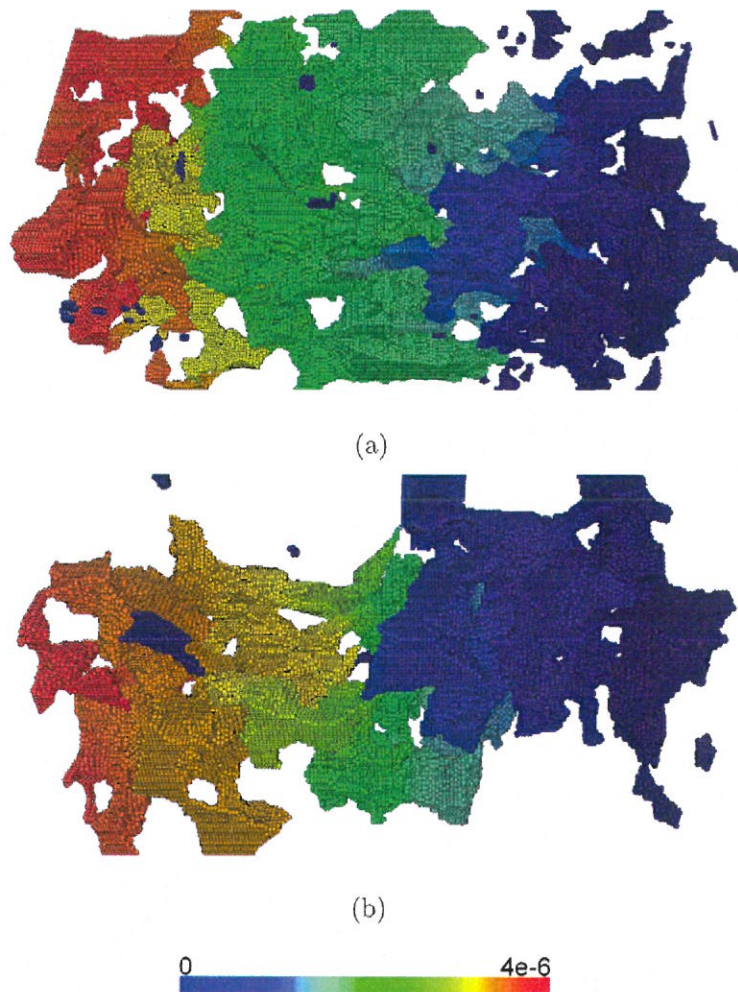

Fig. 1. Pressure distribution in particle representation of (a) sample A from Berea sandstone and (b) sample B from Bentheimer sandstone. Both samples are shown under a 4×10^{-6} Pa pressure difference to further illustrate the pore space.
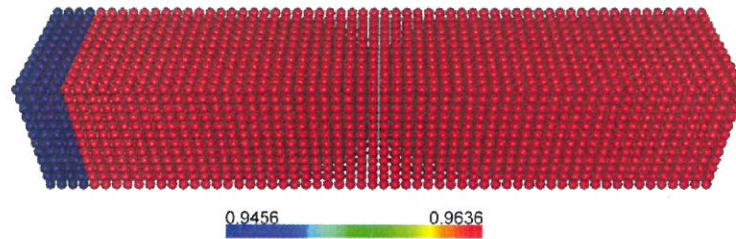
Fig. 2. Mole fraction of water at $t = 0$ in a 24 μm × 24 μm × 120 μm tube with 2 μm resolution used to test the accuracy of the proposed multi-ion transport model.
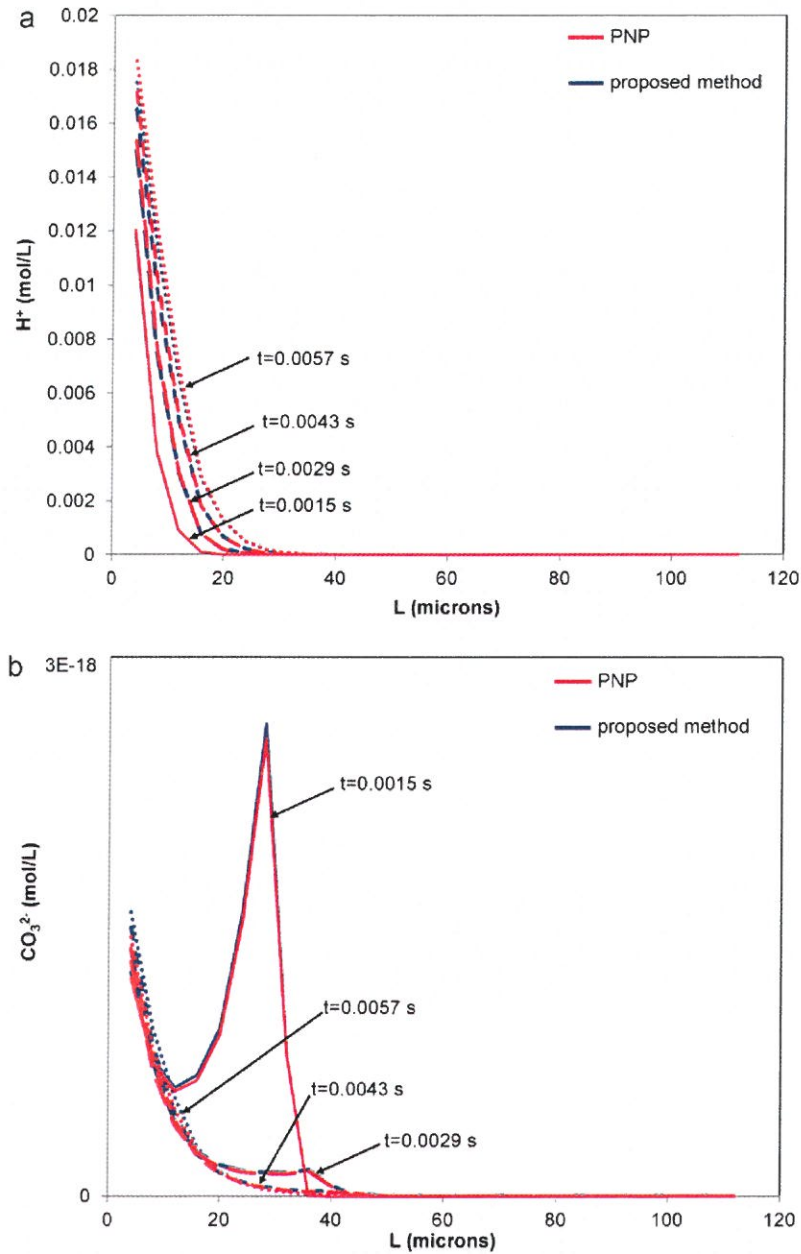

Fig. 3. Comparison of the results obtained using our proposed method against the results obtained after solving the Poisson–Nernst–Planck equations (PNP) for (a) H^+ and (b) CO_3^{2-} concentrations along the length of the test tube at four different times during the simulations.
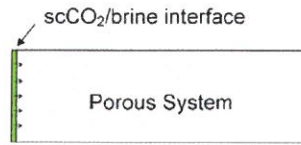
Fig. 4. The scCO₂/brine interface is placed at the inlet of the porous system to allow for molecular diffusion of species across the interface.

particle-based method such as MMPS are the increased stability of flow simulations in disordered porous media as well as a complete erasure of convective term in the governing equations which leads to significant reduction in numerical dispersion. To perform a typical MMPS simulation, after discretizing the voxel image into particles (see Section 2), one needs to detect the particles in the neighborhood of all individual particles (i.e., neighbor search). Then the pressure projection method is used to compute the pressure and velocity fields in the system utilizing a series of summations first introduced by Koshizuka et al. (1995). This information is then used to advance the fluid particles at each time step which leads to a different arrangement of particles and, therefore, necessitates a new neighbor search. This can add an additional computational cost to the simulations when compared to the traditional CFD methods such as finite volume. However, the improved stability of MMPS is often translated into fewer iterations of the pressure solver (Ovaysi and Piri, 2010). Furthermore, depending on how fast the particles move, neighbor search does not need to be carried out at every time step. Consequently, the computational cost of MMPS simulations is comparable to that of the traditional CFD methods.

Dissolution of CO₂ in saline aquifers ensues a series of chemical reactions which in turn produce a number of charged species. Apart from the convective transport of species, which is accounted for by the Navier–Stokes equations, transport of charged species is also controlled by molecular diffusion and electrical coupling forces, i.e.,

$$\frac{DC_i}{Dt} = \left(\frac{DC_i}{Dt}\right)_{diffusion} + \left(\frac{DC_i}{Dt}\right)_{electrical\ coupling} + \left(\frac{DC_i}{Dt}\right)_{chemical\ reactions} \tag{3}$$

where C_i is the concentration of species i.

Based on our simulations, molecular diffusion accounts for close to 70%, electrical coupling less than 30%, and chemical reactions less than 1% of the total transport. Though, these numbers can vary in other cases depending on the reaction rates and diffusion coefficients of the chemical species present in the system. The contribution of molecular diffusion in the overall rate of change for species i in a non-ideal solution is represented by (Marchand et al., 2001)

$$\left(\frac{DC_i}{Dt}\right)_{diffusion} = D_i(\nabla^2 C_i + \nabla \cdot (C_i \nabla \ln \gamma_i)) \tag{4}$$

where D_i is the molecular diffusion coefficient and γ_i is the activity coefficient of species i. We use the Davies equation (Samson et al., 1999) to calculate the activity coefficients of ions. The activity coefficients of neutral species are assumed to be unity. A similar approach as in Ovaysi and Piri (2011) is employed to solve Eq. (4). The non-ideal term in Eq. (4), however, is an addition to the convection–diffusion equation which is also handled by a similar approach as in Ovaysi and Piri (2011).

To account for the electrical coupling of the ions, the conventional approach (Marchand et al., 2001) is to define

$$\left(\frac{DC_i}{Dt}\right)_{electrical\ coupling} = \frac{D_i z_i F}{RT} \nabla \cdot (C_i \nabla \Phi) \tag{5}$$

where z is the charge of the species i, F is Faraday constant, R is gas constant, T is temperature, and Φ is electrostatic potential that is calculated using Poisson's equation, i.e.,

$$\nabla^2 \Phi = -\frac{F}{\epsilon} \sum_i^N z_i C_i \tag{6}$$

where ϵ is the dielectric permittivity of the aqueous phase and N is the number of species. However, due to the large multiplier of F/ϵ on the right-hand-side of Eq. (6), any deviation from the electroneutrality condition of

$$\sum_i^N z_i C_i = 0 \tag{7}$$

will lead to a significant change in the electrostatic field which in turn instantaneously corrects the local ion concentrations in favor
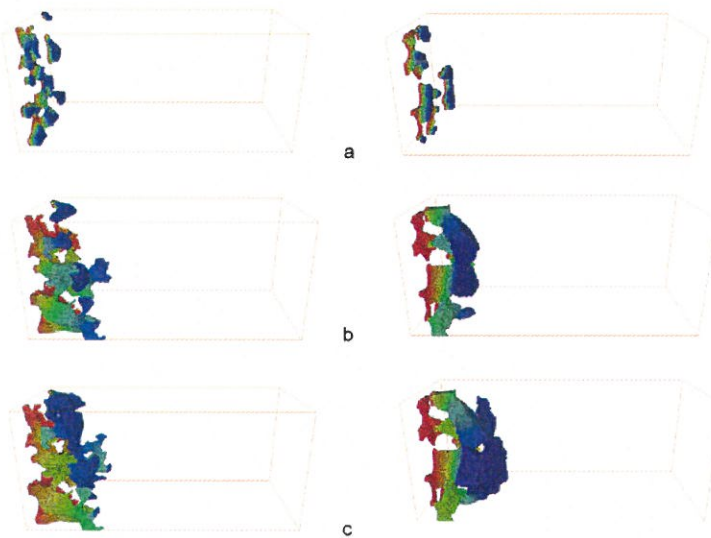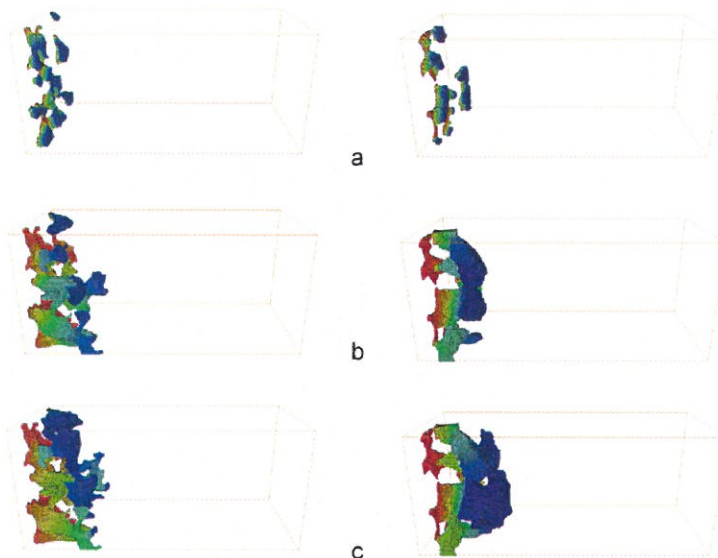

Fig. 5. Progression of the CO₂ plume due to pure CO₂ dissolution in samples A (left) and B (right) at (a) $t = 0.2$ s, (b) $t = 10$ s, and (c) $t = 20$ s. Only the particles with $C_{CO_2} > 0.01$ M at the first 0.65 mm of the samples are shown.

Fig. 6. Progression of the H_2CO_3 plume due to pure CO_2 dissolution in samples A (left) and B (right) at (a) $t=0.2$ s, (b) $t=10$ s, and (c) $t=20$ s. Only the particles with $C_{H_2CO_3} > 0.00017$ M at the first 0.65 mm of the samples are shown.

of Eq. (7). Therefore, Newman and Thomas-Alyea (2004) recommend to solve for only Eq. (7). This would eliminate the need to solve for the system of linear equations arised from Poisson's equation. However, the solution to Eq. (7) is not unique in the presence of more than two ions. Eqs. (5) and (6) guarantee a unique and physically accurate solution to Eq. (7). In practice, however, Eqs. (5) and (6) greatly restrict the time step size, making the simulations computationally very expensive. To overcome this, we recommend Eqs. (8) and (9) presented below in place of Eqs. (5) and (6).

$$\left(\frac{DC_i}{Dt}\right)_{electrical\ coupling} = -\lambda z_i C_i \tag{8}$$

where λ is calculated using

$$\lambda = \frac{\sum_i^N z_i C_i + \Delta t \sum_i^N z_i (DC_i/Dt)_{diffusion}}{\Delta t z_i^2 C_i} \tag{9}$$

which is obtained by combining Eqs. (7), (8), and first-order time integration of C_i. This formulation does not impose any further restriction on the size of time step other than the ones defined by Courant–Friedrichs–Lewy (CFL) condition (Ovaysi and Piri, 2010) which, in the present work, is used to ensure the convergence of the numerical solution to the Navier–Stokes equations. Eqs. (8) and (9) are solved locally for each fluid particle. These equations are implied from Eqs. (5) and (6) by separating the variables z_i and C_i
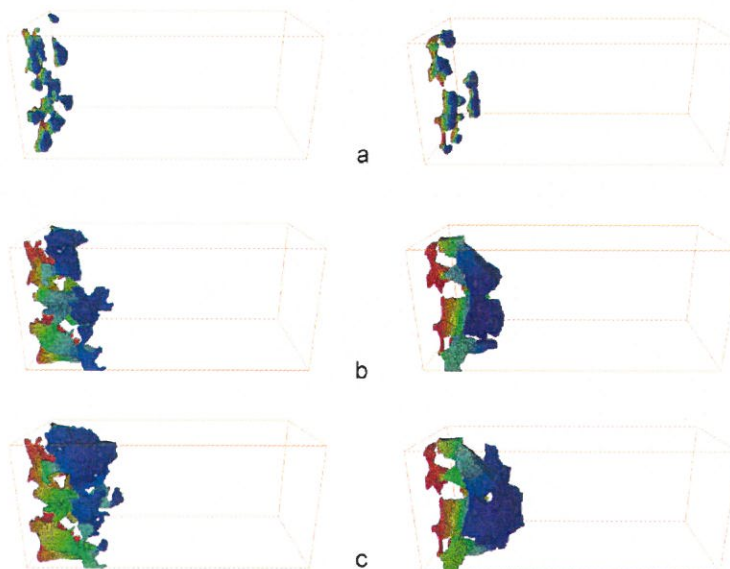

Fig. 7. Progression of HCO_3^- concentration due to pure CO_2 dissolution in samples A (left) and B (right) at (a) $t=0.2$ s, (b) $t=10$ s, and (c) $t=20$ s. Only the particles with $C_{HCO_3^-} > 8.8 \times 10^{-6}$ at the first 0.65 mm of the samples are shown.
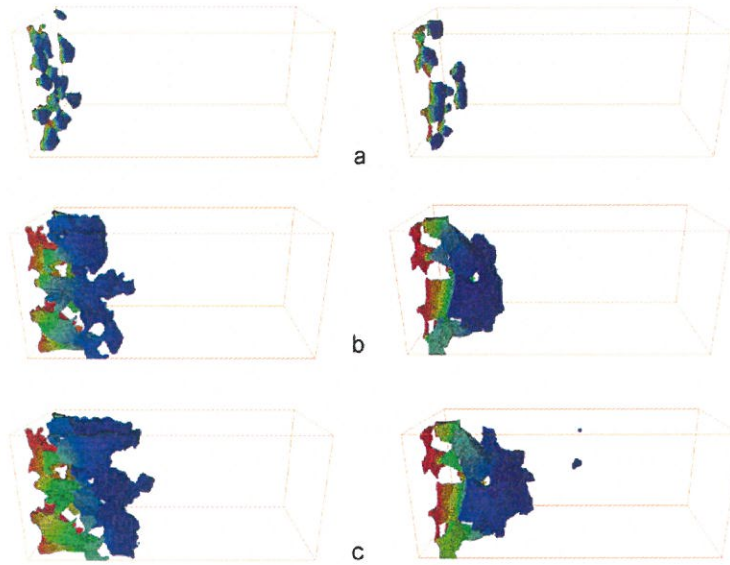
Fig. 8. Progression of CO_3^{2-} concentration due to pure CO_2 dissolution in samples A (left) and B (right) at (a) $t = 0.2$ s, (b) $t = 10$ s, and (c) $t = 20$ s. Only the particles with $C_{CO_3^{2-}} > 5.75 \times 10^{-11}$ at the first 0.65 mm of the samples are shown.

from the rest of the right hand side of Eq. (5) which is constant relative to the concentration of different ions. It should be stressed that Eqs. (8) and (9) are valid only in systems with neutral solid boundaries similar to the systems we study here. Furthermore, these equations are solely developed to expedite the numerical simulations and cannot be used for analytical purposes.

Finally, in Table 3 we list a series of reactions that are believed to ensue following the injection of a mixture of CO_2 and SO_2 in deep saline aquifers (Ellis et al., 2010). We assume the reactions happen instantaneously and therefore, to account for the last term of Eq. (3), we first need to rearrange the reactions in their canonical form (Lichtner et al., 1996). Then, using the stoichiometric relations and the mass action equations for the above-mentioned chemical reactions and also Eq. (3) for all the species, a nonlinear system

of equations is obtained for each fluid particle. The unknowns of this system of equations are $(DC_i/Dt)_{chemical\,reactions}$ for the reactive species which are calculated locally for each fluid particle. For more information on these calculations consult Lichtner et al. (1996).

4. Verification

In a previous study (Ovaysi and Piri, 2010), MMPS has been validated against analytical, numerical, and experimental data available in the literature. In particular, the accuracy of MMPS in capturing the correct velocity field in packed beds was proven. Furthermore, it was shown that MMPS can accurately predict the longitudinal dispersion coefficient in natural porous media under a wide range of Peclet numbers, including the flow regimes
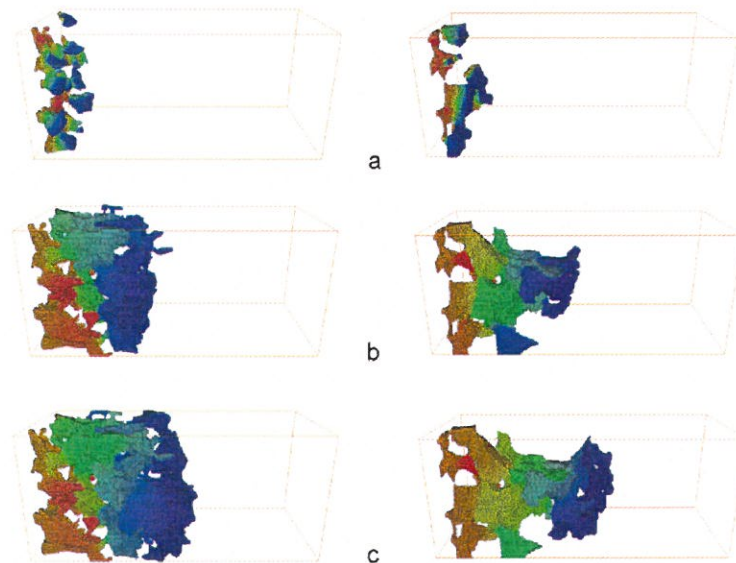

Fig. 9. Progression of pH due to pure CO_2 dissolution in samples A (left) and B (right) at (a) $t = 0.2$ s, (b) $t = 10$ s, and (c) $t = 20$ s. Only the particles with pH < 5.8 at the first 0.65 mm of the samples are shown.
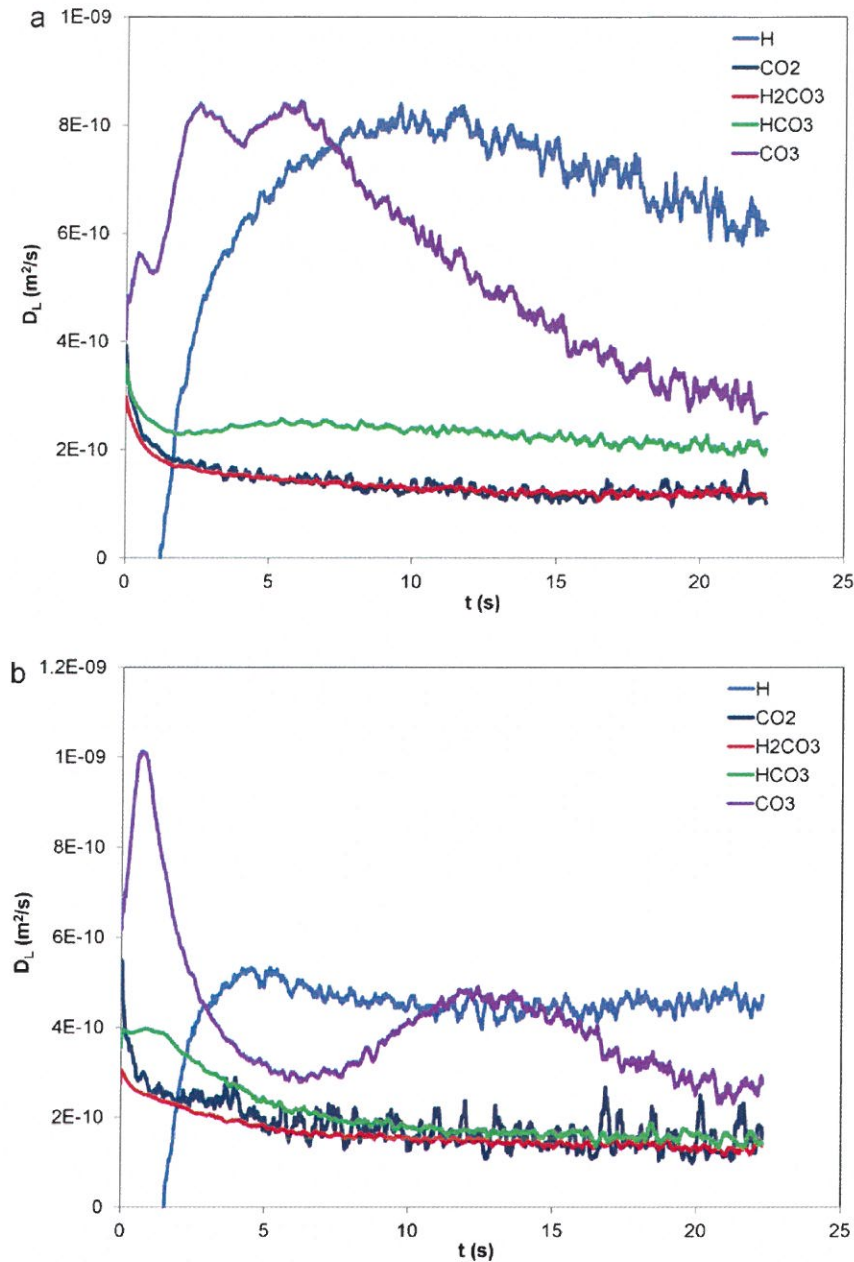
Fig. 10. Evolution of the longitudinal dispersion coefficients of different species due to pure CO_2 dissolution in (a) sample A and (b) sample B.

dominated by inertia and turbulence. The results of that study was successfully compared against the experimental data in the literature in Ovaysi and Piri (2011).

In this paper, in the absence of analytical/experimental data on the transport of multiple ions, we examine the accuracy of our proposed equations, i.e., Eqs. (8) and (9), in capturing the correct physics of multi-ion transport. To do that, we studied the diffusion of a brine saturated with $SO_2 + CO_2$ in a 1 M brine (free of SO_2 and CO_2) at 40 °C and 12.7 MPa, see Table 2 for brine compositions. For this test, we place the $SO_2 + CO_2$ rich brine at the entrance of a 120 μm long tube with square cross section that measures 24 μm at each side, see Fig. 2. The tube is initially filled with the 1 M brine that is free of SO_2 and CO_2. Upon starting the simulations, a series of reactions (see Table 3) ensue that result in the

production of multiple ions as well as few neutral species. Overall, 17 species are present in the system of which 11 are charged. To simplify the comparisons, we only present the concentrations of H^+ and CO_3^{2-} along the length of the tube in Fig. 3. The results of

Table 2
Brine compositions in mol/L.

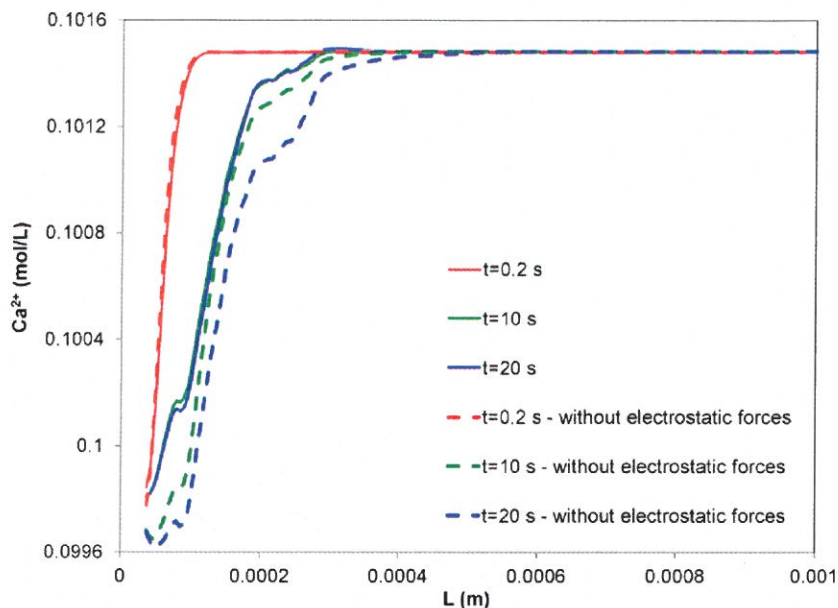| Component	Brine	CO_2 rich brine	$CO_2 + SO_2$ rich brine
H_2O	55.56	55.56	55.56
Na^+	0.8995	0.8975	0.899
Ca^{2+}	0.0998	0.0997	0.0999
Cl^-	1.099	1.0969	1.0988
CO_2	0	0.9972	0.9989
SO_2	0	0	0.0999

Fig. 11. Ca^{2+} profile after pure CO_2 dissolution in sample A in the presence and absence of electrostatic forces.

Table 3
Equilibrium constants taken from Ellis et al. (2010) at 40 °C and 12.7 MPa for 1 M NaCl brine.

Index	Reaction	$\log K_{eq}$
1	$H_2O \Leftrightarrow H^+ + OH^-$	−13.49
2	$SO_2 + H_2O \Leftrightarrow H_2SO_3$	−0.042
3	$H_2SO_3 \Leftrightarrow HSO_3^- + H^+$	−1.93
4	$HSO_3^- \Leftrightarrow SO_3^{2-} + H^+$	−7.24
5	$SO_2 + H_2O \Leftrightarrow \frac{3}{4}HSO_4^- + \frac{3}{4}H^+ + \frac{1}{4}H_2S$	5.68
6	$HSO_4^- \Leftrightarrow SO_4^{2-} + H^+$	−2.12
7	$CO_2 + H_2O \Leftrightarrow H_2CO_3$	−2.77
8	$H_2CO_3 \Leftrightarrow HCO_3^- + H^+$	−6.27
9	$HCO_3^- \Leftrightarrow CO_3^{2-} + H^+$	−10.16

the proposed method are obtained by solving Eq. (3) with the electrical coupling term computed using Eqs. (8) and (9). Whereas, in the Poisson–Nernst–Planck (PNP) case, the electrical coupling term is computed using Eqs. (5) and (6). As shown in Fig. 3 the results obtained using our proposed method are as accurate as those computed using Eqs. (5) and (6). Furthermore, our proposed method does not impose any restriction on the size of the time step leading to faster simulations.

5. Results and discussions

Given its critical temperature and pressure (31.1 °C and 7.38 MPa), CO_2 will exist as a supercritical fluid in deep saline aquifers. In this section, we study the dissolution of supercritical CO_2 phase (scCO$_2$) in brine. To do that, we first saturate the

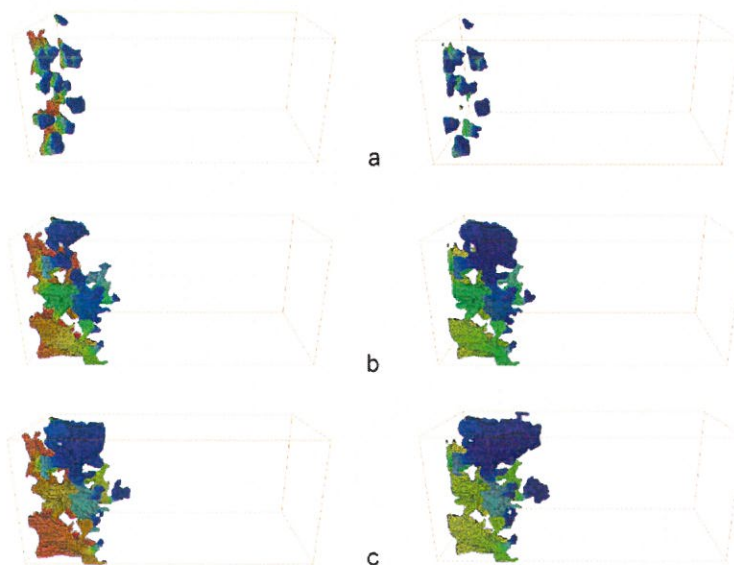**Fig. 12.** Progression of pH due to $CO_2 + SO_2$ dissolution in sample A in the presence (left) and absence (right) of electrostatic forces at (a) $t = 0.2$ s, (b) $t = 10$ s, and (c) $t = 20$ s. Only the particles with pH < 2.53 at the first 0.65 mm of the sample are shown.
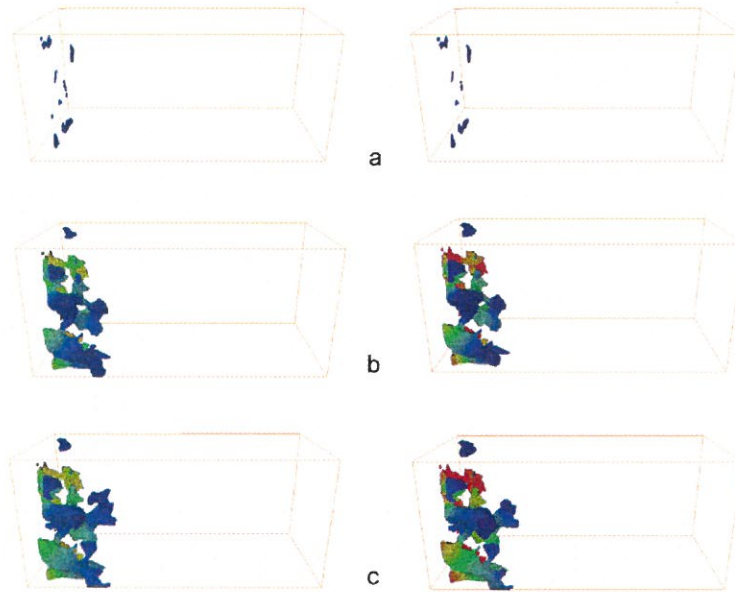
Fig. 13. Progression of HSO_4^- due to $CO_2 + SO_2$ dissolution in sample A in the presence (left) and absence (right) of electrostatic forces at (a) $t = 0.2$ s, (b) $t = 10$ s, and (c) $t = 20$ s. Only the particles with $C_{HSO_4^-} > 0.0086$ M at the first 0.65 mm of the sample are shown.

samples A and B with 1 M neutral brine. We then, as shown in Fig. 4, introduce the brine solution equilibrated with CO_2 (or $CO_2 + SO_2$) at the inlet of the sample, see Table 2 for brine compositions. The assumption is that the $scCO_2$/brine interface is located at the inlet of the sample (left side in Fig. 1(a) and (b)) and is constantly feeding the sample with CO_2 (or $CO_2 + SO_2$) saturated brine solution. The CO_2 and SO_2 solubilities in the brine solution are based on the data reported by Ellis et al. (2010) which are calculated for 1 M brine at 40 °C and 12.7 MPa. Also, Table 4 lists the molecular diffusion coefficients used in the present study. To simulate a realistic scenario, we establish a background aquifer velocity of 10 cm/yr (3×10^{-9} m/s) (Bachu et al., 1994) by applying 8×10^{-6} Pa and 4×10^{-6} Pa

Table 4
Molecular diffusion coefficients of different ions in water at 40 °C taken from Newman and Thomas-Alyea (2004) and Ellis et al. (2010).

Species	D_m (m²/s) $\times 10^9$	Species	D_m (m²/s) $\times 10^9$
H^+	9.312	HCO_3^-	1.24
OH^-	5.26	CO_3^{2-}	0.968
Na^+	1.334	H_2SO_3	2.31
Ca^{2+}	0.792	HSO_3^-	1.62
Cl^-	2.032	SO_3^{2-}	1.01
CO_2	1.94	HSO_4^-	1.45
SO_2	2.316	SO_4^{2-}	1.12
H_2CO_3	1.5	H_2S	1.93

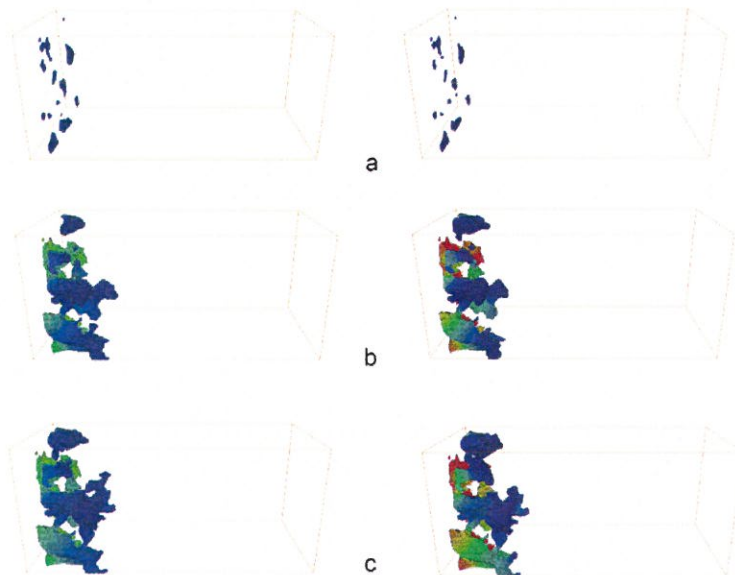**Fig. 14.** Progression of SO_4^{2-} due to $CO_2 + SO_2$ dissolution in sample A in the presence (left) and absence (right) of electrostatic forces at (a) $t = 0.2$ s, (b) $t = 10$ s, and (c) $t = 20$ s. Only the particles with $C_{SO_4^{2-}} > 0.0032$ M at the first 0.65 mm of the sample are shown.

pressure difference across samples A and B, respectively. This yields a very low Peclet number, i.e., Pe < 1 × 10^{-4}, which places the dispersion regime in a zone dominated by molecular diffusion in both samples A and B. In practice, the above conditions prevail when the CO_2 stored through residual and structural trapping gets exposed to fresh brine due to small background velocity of the acquifer. In both cases, the supercritical phase gradually shrinks by diffusing into the surrounding aqueous phase at very low Peclet numbers. Also, to speedup the simulations that follow, we used a multi-GPU accelerated code (Ovaysi and Piri, 2012) that was developed recently.

5.1. Pure CO_2 dissolution

Shown in Fig. 5 is the visualization of CO_2 dispersion in the brine phase in samples A and B. Following the reaction route specified in Table 3, H_2CO_3 is formed in the presence of CO_2, see Fig. 6. Carbonic acid then dissociates in two stages to give H^+, HCO_3^-, and CO_3^{2-} ions. The bicarbonate and carbonate ions reach their peak concentrations at the inlet of the sample with a gradual dilution towards the outlet as seen in Figs. 7 and 8. Noteworthy in these figures, despite having an inferior molecular diffusion coefficient, the carbonate ions spread faster than the bicarbonate ions. To further investigate this, we show pH progression in these samples in Fig. 9. As expected, the hydrogen ions spread faster due to their much higher molecular diffusion coefficient compared to all the other ions present in the system, see Table 4. However, their dispersion rate is compromised by reactions (8) and (9) listed in Table 3. A closer look at Figs. 6, 7 and 9 reveals that the H^+ produced by reactions (8) and (9) quickly disperses throughout the system. This further shifts these reactions to the right in favor of production of the HCO_3^- and CO_3^{2-} ions. The HCO_3^- ion, however, is further consumed in reaction (9) leading to an overall lower dispersion rate for HCO_3^- compared to that of CO_3^{2-}.

Due to the low background velocity, molecular diffusion is dominant in both samples and hence pore connectivity does not play a major role in the transport of species. Therefore, transport of the species in both samples A and B are comparable. The only exception is distribution of the low pH (more acidic) particles in the samples. As clearly seen in Fig. 9, low pH particles at the inlet of sample A are more pronounced compared to those in sample B. This is due to the superior connectivity of sample B which creates a medium where H^+ ions come in better contact with a fresh supply of neutral brine far from the interface. This helps to further neutralize the acidic front in the more conductive fluid channels of both samples A and B, though, sample B has a higher density of conductive fluid channels. Acidity of the less conductive or dead-end fluid channels which are more present in sample A, on the other hand, remains high throughout the simulations which could indicate a higher chance for mineral reactions in these areas.

Using the method of moments as described in Ovaysi and Piri (2011), we have computed the longitudinal dispersion coefficients for the different species. Fig. 10 illustrates variation of the longitudinal dispersion coefficients versus time for CO_2, H_2CO_3, H^+, HCO_3^-, and CO_3^{2-} in samples A and B. It should be noted that, due to their extremely low velocities, none of the fluid particles enters the downstream section during the 20 s simulations. Therefore, concentration in the downstream section, which is equal to the original brine concentration, remains fixed throughout the simulation. Consequently, a steady-state concentration profile establishes between the two fixed boundaries at the inlet and outlet. This leads to a zero rate of growth for the plume and hence a zero rate of dispersion after steady state is reached. Also, the plotted values in these figures are strongly influenced by the reactions listed in Table 3 and hence a slightest change in the concentration of
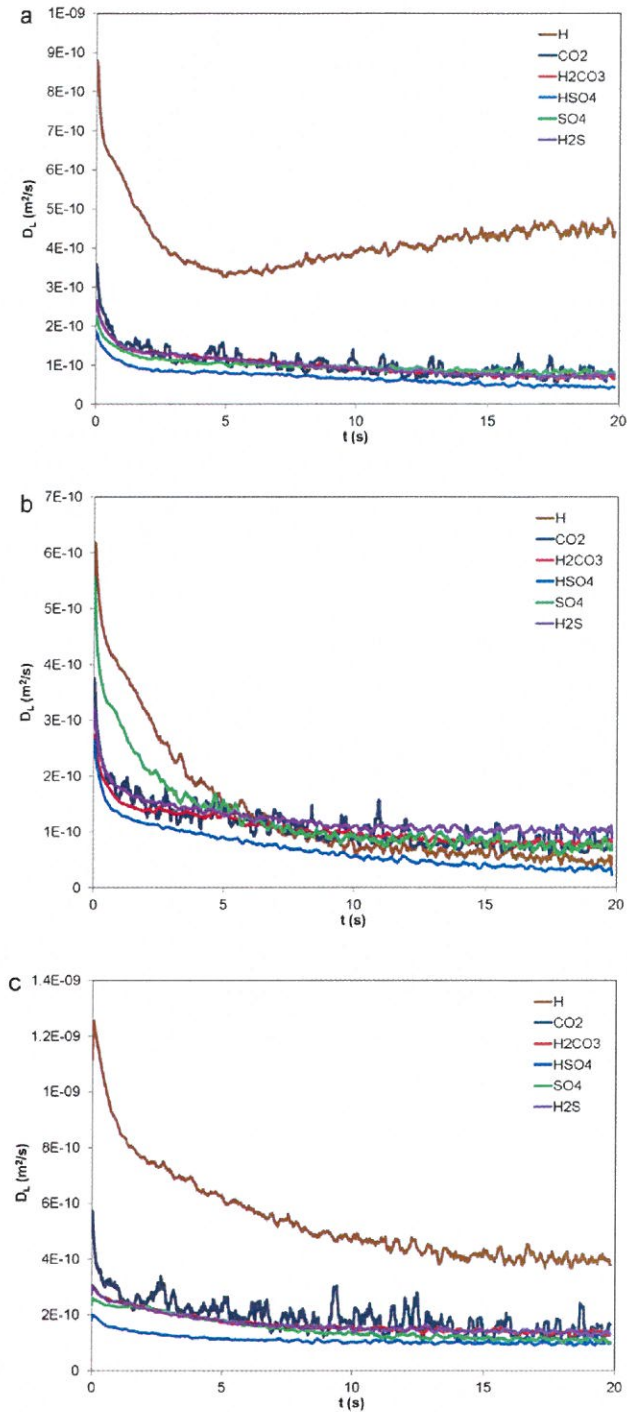

Fig. 15. Evolution of the longitudinal dispersion coefficients of different species resulting from $CO_2 + SO_2$ dissolution in (a) sample A in the absence of electrostatic forces, (b) sample A, and (c) sample B.

one species triggers a redistribution of other species. As such, the computed dispersion coefficients in Fig 10 can be used as a tool to assess the reactivity of the species. For instance, according to reaction number 7 in Table 3, H_2CO_3 is produced when CO_2 comes in contact with water. Therefore, since water is present everywhere in the pore space, presence of the dissolved CO_2 translates to the
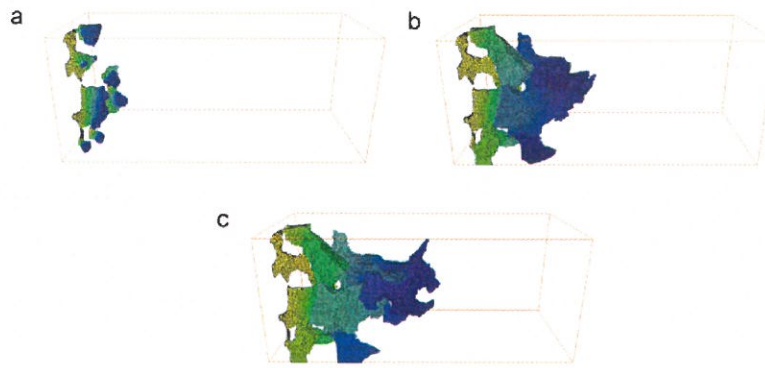
Fig. 16. Progression of pH due to $CO_2 + SO_2$ dissolution in sample B at (a) $t = 0.2$ s, (b) $t = 10$ s, and (c) $t = 20$ s. Only the particles with pH < 2.53 at the first 0.65 mm of the sample are shown.

presence of H_2CO_3 which is also supported by Figs. 5 and 6 for samples A and B. This explains why the computed dispersion coefficients of these two components overlap throughout the simulation for both samples. As explained earlier, dispersion rate of the bicarbonate and carbonate ions are increased due to the fast dispersion of the hydrogen ions and the dissociation reactions of carbonic acid. In fact, dispersion of the bicarbonate and carbonate ions is primarily controlled by the dispersion pattern of the hydrogen ion. This can be better understood by studying the pH front in Fig. 9 at $t = 10$ s where the hydrogen ions are introduced to large pores in the middle of sample B. According to Ovaysi and Piri (2011), this translates to a slight increase in the dispersion coefficient of H^+ as similar features in the sample have already been scanned by the plume of H^+. Since H^+ passes quickly through this conductive area of sample B, the balance of both reactions (8) and (9) is shifted more to the right which results in an increase in CO_3^- production and hence an increase in its dispersion coefficient as calculated in the present work. However, passage of the hydrogen ion through this conductive area is quick and the next fluid channels are not as

conductive leading to less dispersion of the hydrogen ions and consequently slower production of the carbonate ions. Overall, the net result of this interaction is a pulse of CO_3^{2-} production that results in a peak for the longitudinal dispersion coefficient of carbonate ions.

To investigate the impact of electrostatic forces on distribution of the different ions present in the system, we also simulated the dissolution of scCO$_2$ in sample A in the absence of the electrical coupling term in Eq. (3). Knowing that the system is electroneutral at $t = 0$, the only factor to change the balance of the electrostatic forces is production of the cations and anions resulting from dissociation of carbonic acid. However, carbonic acid's rate of dissociation is very low and the produced ions are in very small quantities. Therefore, no detectable change in the distribution of H^+, HCO_3^-, or CO_3^{2-} was observed in the absence of the electrostatic forces. Nonetheless, production of H^+, and particularly its fast rate of dispersion, slightly impacted the distribution of Ca^{2+} at the inlet of the sample, see Fig. 11. It is evident from this figure that, in the presence of electrostatic forces, the hydrogen cations repel the
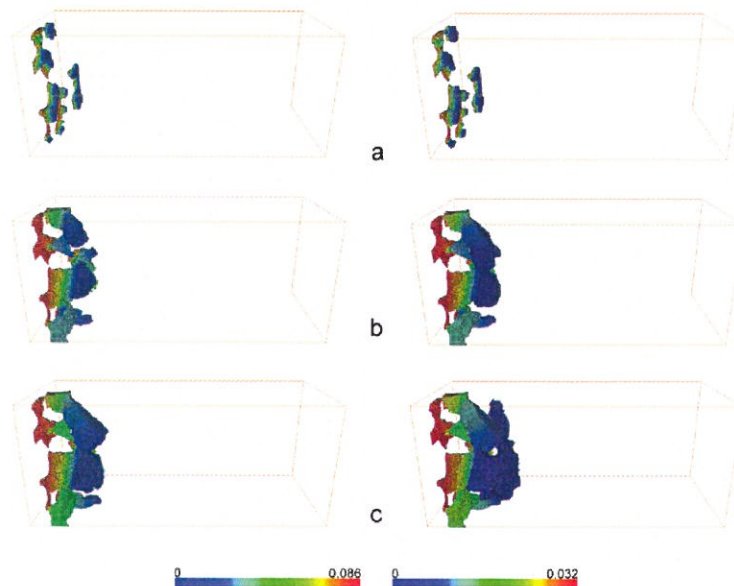

Fig. 17. Progression of HSO_4^- (left) and SO_4^{2-} (right) due to $CO_2 + SO_2$ dissolution in sample B at (a) $t = 0.2$ s, (b) $t = 10$ s, and (c) $t = 20$ s. Concentrations are in molar. Only the particles with $C_{HSO_4^-} > 0.0086$ M (left) or $C_{SO_4^{2-}} > 0.0032$ M (right) at the first 0.65 mm of the sample are shown.
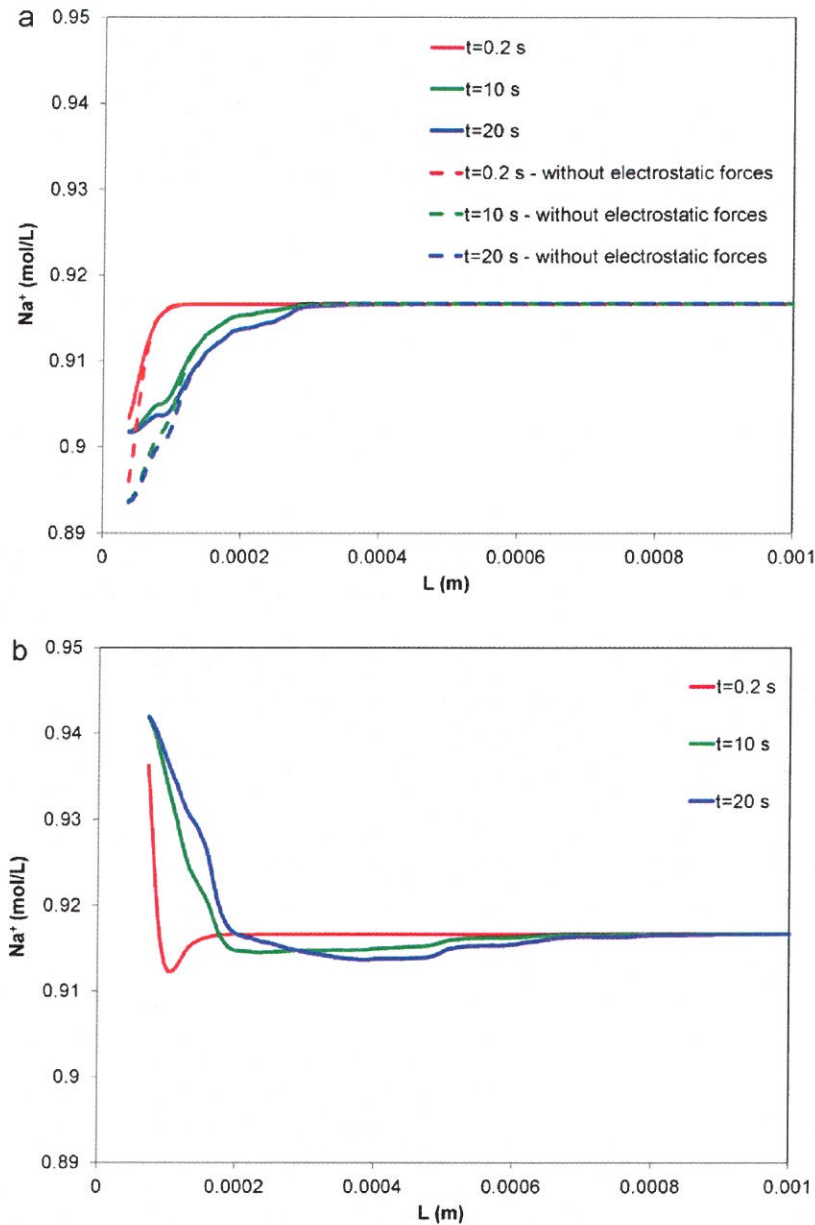
Fig. 18. Evolution of Na$^+$ concentration resulting from $CO_2 + SO_2$ dissolution in (a) sample A in the presence and absence of electrostatic forces, and (b) sample B.

divalent calcium cations leading to a sharp increase in Ca^{2+} concentration at the inlet of the sample. This repulsion force, however, is negligible on Na$^+$ for two reasons: First, Na$^+$ is present in much higher concentrations than Ca^{2+} and the very weak repulsion forces from a dilute solution of H$^+$ cannot cause significant change in the saturation of Na$^+$; Second, Na$^+$ is monovalent and receives a smaller repulsion force from H$^+$ compared to the repulsion force exerted on the divalent Ca^{2+}. Also, no significant change was observed in the concentration of Cl$^-$ in the absence of electrostatic forces. This can be attributed to the high concentration of Cl$^-$ compared to the low quantities of H$^+$ produced in the system. We also see a decrease in Ca^{2+} concentration at the inlet of the sample in the absence of the electrostatic forces. This is caused due to the production of other species in the system which leads to the dilution of Ca^{2+} at the inlet.

5.2. CO_2 and SO_2 dissolution

Based on the emission data published in Miller and Van Atten (2004), a 99% CO_2 and 1% SO_2 composition was chosen for the scCO$_2$ phase which comes in contact with the brine phase at the inlet of the samples. This composition, however, is greatly altered in the brine phase due to the vastly different solubilities of CO_2 and SO_2 in brine. Composition of the $CO_2 + SO_2$ saturated brine, which represents the scCO$_2$/brine interface and is placed at the inlet of the samples, is listed in Table 2. Once this interface comes in contact with the brine solution, SO_2 is entirely consumed in the hydrolysis and disproportionation reactions that ensue and its saturation is not detectable in any of the samples. As shown in Fig. 12 the high dissociation rate of sulfuric acid leads to the formation of a strongly acidic front in sample A. Besides H$^+$, progression of the
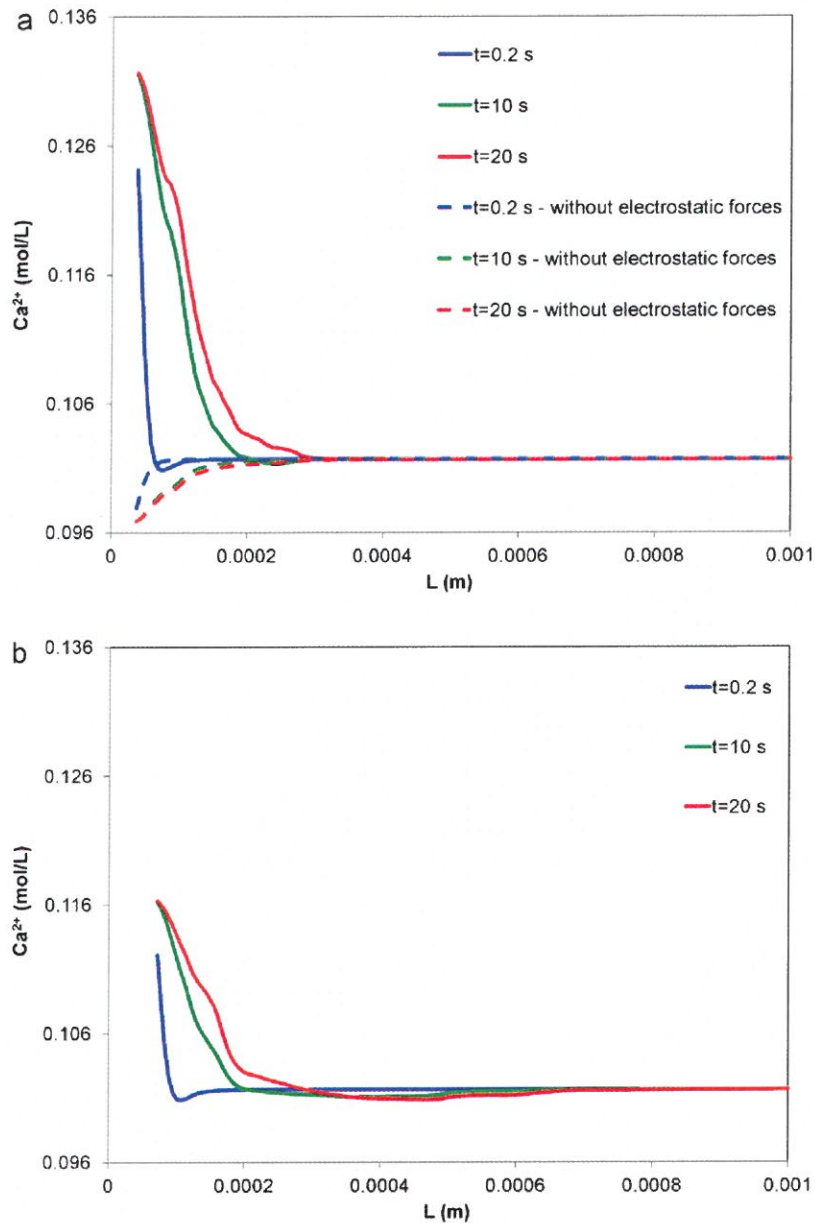
Fig. 19. Evolution of Ca^{2+} concentration resulting from $CO_2 + SO_2$ dissolution in (a) sample A in the presence and absence of electrostatic forces, and (b) sample B.

other products of sulfuric acid dissociation, i.e., HSO_4^- and SO_4^{2-}, in sample A are shown in Figs. 13 and 14, respectively. To study the impact of electrostatic forces on the distribution of these anions, similar to the study in Section 5.1, we also carried out a second simulation in sample A for $CO_2 + SO_2$ dissolution in the absence of the electrical coupling term in Eq. (3). In the above figures, we also illustrate the progression of the hydrogen, bisulfate, and sulfate ions in sample A in the absence of electrostatic forces where we notice a decline in the concentration of H^+ (increase in pH) and an increase in the concentration of both HSO_4^- and SO_4^{2-}. This can be explained by the vastly different molecular diffusion coefficients of the hydrogen cation compared to those of the bisulfate and sulfate anions. In the absence of electrostatic forces, these ions diffuse independently which means that H^+ quickly diffuses away from its production site, leaving behind a dilute solution of H^+.

On the other hand, HSO_4^- and SO_4^{2-} which have much smaller molecular diffusion coefficients stay close to their production sites. This yields a higher concentration for these ions in the absence of electrostatic forces. However, in reality, the electrostatic forces are present which requires the cations and anions to be coupled, leading to a slower rate of diffusion for H^+ and a faster rate of diffusion for HSO_4^- and SO_4^{2-}. Consequently, compared to the case in which the electrostatic forces were ignored, H^+ stays closer to its production site, i.e., primarily the inlet, and HSO_4^- and SO_4^{2-} move away from the inlet faster. Interestingly, the maximum HSO_4^- concentration observed in the presence of electrostatic forces is 30% smaller than that obtained in the absence of electrostatic forces. In the case of SO_4^{2-}, this number is 60%. Considering these values, it is evident that the divalent sulfate anion has received a twice stronger pull from the hydrogen cation compared to the pull on the monovalent
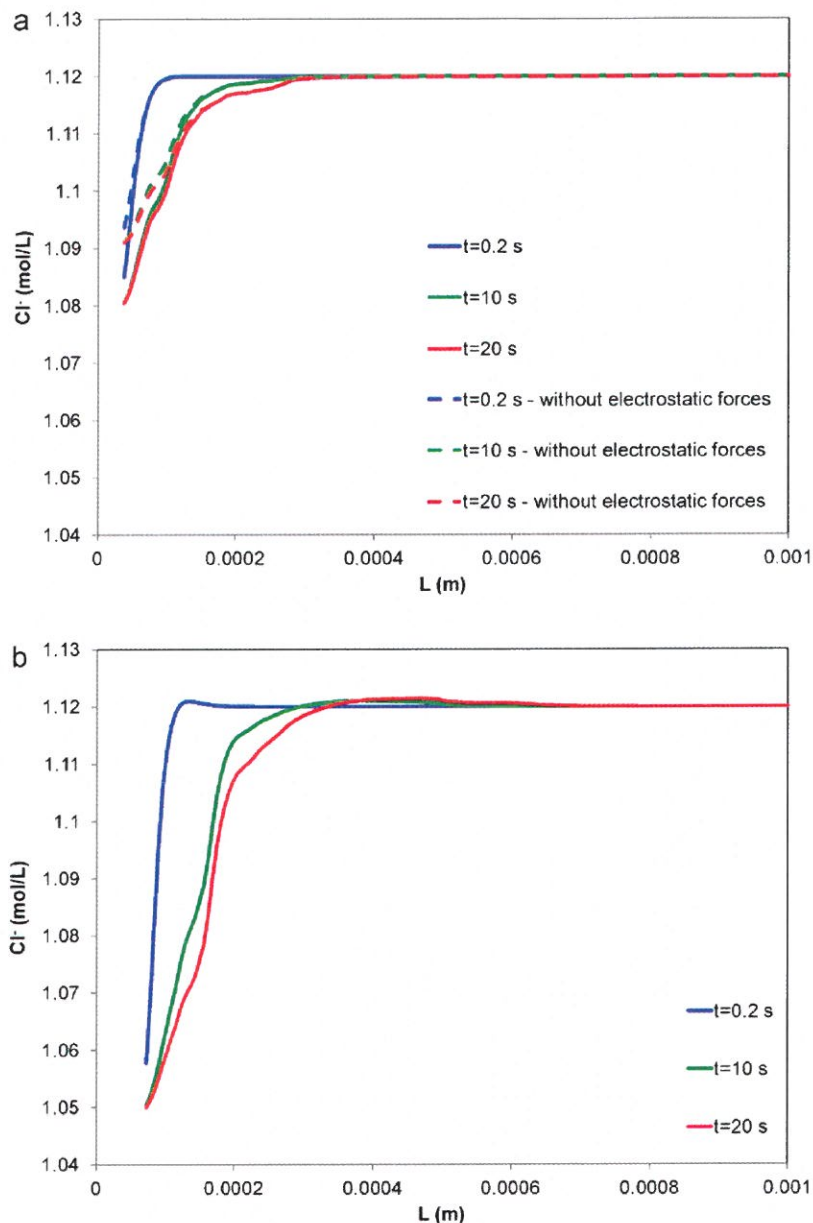
Fig. 20. Evolution of Cl⁻ concentration resulting from $CO_2 + SO_2$ dissolution in (a) sample A in the presence and absence of electrostatic forces, and (b) sample B.

bisulfate anion. The graphs in Fig. 15 support the statements above where, in the presence of electrostatic forces, longitudinal dispersion coefficient of H^+ has inched above those of HSO_4^- and SO_4^{2-}. It is also clear that in the presence of electrostatic forces, the electrical coupling of the ions leads to a greater variation of their respective dispersion coefficients. However, since the dispersion coefficients continuously decline towards zero, no conclusive remarks can be made regarding how the electrostatic forces might influence the time scale of asymptotic behavior.

Another factor contributing to the formation of a highly acidic area at the inlet of sample A is the poor connectivity of this sample. The produced hydrogen ions in sample A are mostly trapped at the inlet, due to the very turtuous network of fluid channels existing in this sample. On the contrary, fluid channels in sample B are not only better connected but also wider, which provide a more efficient

pathway for the produced species to travel away from their production sites. Evolution of pH in sample B is shown in Fig. 16 where the low pH front has scanned more length of the sample compared to that in sample A. Also, a better dispersion of the hydrogen ions in sample B has translated to a rather dilute solution of H^+ at the inlet. Furthermore, as shown in Fig. 17, compared to sample A, concentration of the bisulfate and sulfate ions at the inlet remain higher in sample B. This can be explained by the concentration profile of other ions present in the system, namely the mineral ions of Na^+, Ca^{2+}, and Cl^-. As shown in Figs. 18–20, these ions are distributed quite differently in samples A and B. We use the profile of these ions in the absence of electrostatic forces as a base case where the mineral ions are not altered by these forces. In sample A, due to its poor connectivity, the produced ions cannot move considerably and hence are forced to neutralize their electrical charge by

themselves. This has led to less alteration of the mineral ions, except for Ca^{2+} which, as explained earlier in Section 5.1, is a divalent cation that exists in smaller quantities and therefore more susceptible to alteration. In sample B, on the other hand, the produced ions are not restricted by porous system and therefore can rely on the existing mineral ions in the system to reach an electroneutral state. Therefore, in sample B, H^+ does not need to couple with HSO_4^- and SO_4^{2-}. Hence, as shown in Fig. 15, the hydrogen cation can disperse faster as the mineral ions are present throughout the system. However, this alters the concentration of the mineral ions in areas away from the inlet as seen in Figs. 18–20. The slow diffusing bisulfate and sulfate anions, also, are less dependent on the hydrogen cation and instead couple with the mineral ions at the inlet of sample B.

Being a neutral component, identical to Section 5.1, CO_2 diffuses throughout both samples A and B to produce H_2CO_3. However, due to its low dissociation rate, the produced carbonic acid acts as a buffer for sulfuric acid. Therefore, both the bicarbonate and carbonate ions are present only in trace quantities of less than 10^{-12} M. Though, these ions are even less present in sample B due to the fact that H^+ is strongly present throughout the system. Therefore, the diffused CO_2 in the presence of SO_2 can only give H_2CO_3. Since, most of the diffused SO_2 is consumed in the production of sulfuric acid, sulfurous acid is rarely produced. Even then, this weak acid acts as another buffer for sulfuric acid. Hence, sulfurous acid and its dissociation products are not present in any of the samples in noticeable quantities.

6. Conclusions

In this study, the particle-based method of MMPS was extended to model reactive multi-ion transport of charged and neutral species resulting from the dissolution of CO_2 and $CO_2 + SO_2$ in deep saline aquifers. We observed that, in the case of pure CO_2 dissolution, a weakly acidic front (pH $\simeq$ 4.8) establishes at areas close to the scCO$_2$/brine interface. This acidic front spreads throughout the system, though at a faster rate in samples with good connectivity. Since the produced ions resulting from the dissolution of pure CO_2 are in small quantities, the electrostatic forces only slightly affect the transport of species. Dissolution of $CO_2 + SO_2$, on the other hand, leads to the production of large quantities of charged species which are significantly influenced by the electrostatic forces. These forces can then greatly alter the mineral makeup of the brine, a phenomenon that cannot be observed in the absence of electrostatic forces. We also observed that the highly acidic front (pH $\simeq$ 1.53) is firmly maintained in porous media with poor connectivities. In addition to using a multi-GPU accelerated code, to expedite the simulations, we also chose relatively small subsets of the two sandstones studied here. Although previous studies

(Ovaysi, 2010) indicate improved connectivity in larger samples (for samples smaller than REV size), based on the early results of our simulations on larger samples, we believe these small subsets offer enough pore-scale details to examine the physics of multi-ion transport at this scale. We intend to extend the current model to include mineral reactions which would eventually help improve the current understanding of CO_2 trapping mechanisms and hence lead to the design of better optimized CO_2 sequestration strategies.

References

Bachu, S., Gunter, W.D., Perkins, E.H., 1994. Aquifer disposal of CO$_2$: hydrodynamic and mineral trapping. Energy Conversion and Management 35, 269–279.

Dong, H., 2007. Micro-CT imaging and pore network extraction. Ph.D. Diss. Dep. Earth Sci. Eng., Imperial College, London.

Ellis, B.R., Crandell, L.E., Peters, C.A., 2010. Limitations for brine acidification due to SO$_2$ co-injection in geologic carbon sequestration. International Journal of Greenhouse Gas Control 4, 575–582.

Flukiger, F., Bernard, D., 2009. A new numerical model for pore scale dissolution of calcite due to CO$_2$ saturated water flow in 3D realistic geometry: principles and first results. Chemical Geology 265, 171–180.

Kang, Q., Tsimpanogiannis, I.N., Zhang, D., Lichtner, P.C., 2005. Numerical modeling of pore-scale phenomena during CO$_2$ sequestration in oceanic sediments. Fuel Processing Technology 86, 1647–1665.

Koshizuka, S., Tamako, H., Oka, Y., 1995. A particle method for incompressible viscous flow with fluid fragmentation. Computational Fluid Dynamics Journal 4 (1), 29–46.

Li, L., Steefel, C.I., Yang, L., 2008. Scale dependence of mineral dissolution rates within single pores and fractures. Geochimica et Cosmochimica Acta 72, 360–377.

Lichtner, P.C., Steefel, C.I., Oelkers, E.H., 1996. Reactive Transport in Porous Media, Reviews in Mineralogy, vol. 34. Mineralogical Society of America.

Lopez, O., Idowu, N., Mock, A., Rueslatten, H., Boassen, T., Leary, S., Ringrose, P., 2011. Pore-scale modelling of CO$_2$-brine flow properties at In Salah, Algeria. Energy Procedia 4, 3762–3769.

Marchand, J., Samson, E., Beaudoin, J.J., 2001. Modeling Ion Transport Mechanisms in Unsaturated Porous Media. Institute for Research in Construction.

Miller, P.J., Van Atten, C., 2004. North American Power Plant Air Emissions. Commission for Environmental Cooperation of North America, Montreal, Canada.

Newman, J., Thomas-Alyea, K.E., 2004. Electrochemical Systems. John Wiley & Sons, Inc., Hoboken, NJ.

Ovaysi, S., Piri, M., 2010. Direct pore-level modeling of incompressible fluid flow in porous media. Journal of Computational Physics 229, 7456–7476.

Ovaysi, S., 2010. Direct pore-level modeling of fluid flow in porous media. Ph.D. Diss. Dep. Chem. Pet. Eng., University of Wyoming.

Ovaysi, S., Piri, M., 2011. Pore-scale modeling of dispersion in disordered porous media. Journal of Contaminant Hydrology 124, 68–81.

Ovaysi, S., Piri, M., 2012. Multi-GPU acceleration of direct pore-scale modeling of fluid flow in natural porous media. Computer Physics Communications 183, 1890–1898.

Samson, E., Lemaire, G., Marchand, J., Beaudoin, J.J., 1999. Modeling chemical activity effects in strong ionic solutions. Computational Materials Science 15, 285–294.